

Magic distances for flat bands in twisted bilayer graphene

Antonio Palamara,^{1,2,*} Michele Pisarra,^{1,2,†} and Antonello Sindona^{1,2,‡}

¹*Dipartimento di Fisica, Università della Calabria,
Via P. Bucci, Cubo 30C, I-87036 Rende (CS), Italy*

²*INFN, sezione LNF, Gruppo collegato di Cosenza,
Via P. Bucci, Cubo 31C, I-87036 Rende (CS), Italy*

Twisted bilayer graphene is known to host isolated and relatively flat bands near charge neutrality, when tuned to specific *magic* angles. Nonetheless, these rotational misalignments, lying below 1.1 degrees, result in long-period moiré crystals, whose anomalous electronic properties are hardly accessible to reliable atomistic simulations. Here, we present a map of differently stacked graphene sheets, at arbitrary rotation angles corresponding to precise interplanar distances, into an equivalence class represented by *magic-angle* twisted bilayer graphene. We determine the equivalence relation in the class within a continuum model, and extend its definition to a tight-binding approach. Then, we use density functional theory to suggest that the *magic-angle* physics may be characterized by costly computational strategies on a twisted bilayer geometry, with conveniently large stacking angles. Our results may pave the way for an ab initio characterization of the unconventional topological phases and related excitations, associated with currently observed low-energy quasi-flat bands.

I. INTRODUCTION

Twisted bilayer graphene (TBG) refers to a unique structure formed by stacking two graphene layers on top of each other, at given distance and rotational mismatch, which offers an intriguing mixture of electronic and geometric effects. In particular, the TBG lattice develops large moiré patterns for some *magic* twist angles, exhibiting strongly-correlated phenomena, such as unconventional Mott insulator, Chern insulator and superconducting phases [1–6]. These features are associated with the appearance of nearly flat bands with vanishing group velocity at the Fermi level, as predicted by theory [7–10], and subsequently observed in a number of seminal experiments [11–16].

The discovery of so-called *magic-angle* (MA) TBG has spawned the field of twistronics [17, 18]. Furthermore, MATBG has widened the already rich field of Van der Waals (VdW) heterostructures [19], by introducing a new degree of freedom in the ability to assemble different two-dimensional (2D) materials through VdW interactions, with on-demand electronic, mechanical, and thermal properties.

Nonetheless, the misalignment angle θ between the graphene sheets is not the only geometric parameter responsible for the formation of quasi-flat bands. The interlayer distance d also plays an equally crucial role in the development of these non-dispersive electronic states. Indeed, quasi-flat bands can also be achieved by applying vertical pressures, of the order of the gigapascal, to the layers of a non-magic-angle TBG system [20–24]. In the simplest picture [7], the emergence of quasi-flat bands

arises from the interplay of two energy scales. One involves the electronic states over the moiré superlattice sites, and is determined by θ . The other reflects the coupling between the lattice sites of the TBG layers, and depends on d .

Unfortunately, the unique features of MATBG are commonly observed at very small twist angles $\theta \sim 1.1^\circ$, corresponding to supercell sizes of $\sim 10^4$ atoms, which turns into a formidable challenge for the modeling community. On these premises, we here discuss the existence of an infinite set of crystal (and arguably quasi-crystal) structures, determined by different values of θ associated to precise values of d , which belong to an equivalence class, with MATBG serving as a representative member. The map between elements of the class may allow a thorough investigation of the magic-angle quasi-flat-band physics, by focusing on the most convenient geometry within the class accessible to atomistic simulation methods. Other mappings are available that allow to effectively reduce the unit cell size of a TBG moiré crystal [25–28]. However, they are defined in specific tight binding (TB) models by operating on its free parameters. Our approach, on the other hand, stems from an experimentally observable quantity, i.e., the interlayer distance or the twist angle, being thus independent of the underlying theory.

The remainder of this paper is organized as follows. In Sec. II, we introduce the equivalence class within a continuum model (CM) approach [7, 8, 29–32]. In Sec. III, we extend the map to a TB formulation [33]. In Sec. IV, we suggest how the equivalence relation can be used in density-functional theory (DFT) to access the Kohn-Sham (KS) spectrum of TBG at the smallest magic-angle. Finally, in Sec. V, we outline a possible application of our results on the time-dependent (TD) DFT treatment of MATBG.

* antonio.palamara@unical.it

† michele.pisarra@fis.unical.it

‡ antonello.sindona@fis.unical.it

II. THE EQUIVALENCE CLASS OF MATBG

The CM provides a simple way to study and predict the emergence of quasi-flat bands in a TBG of stacking angle θ . Such an approach is based on the single-valley Hamiltonian

$$\mathcal{H} = \begin{bmatrix} v_F \boldsymbol{\sigma}_{\theta/2} \cdot \mathbf{p} & \mathcal{T}(\mathbf{r}) \\ \mathcal{T}(\mathbf{r})^\dagger & v_F \boldsymbol{\sigma}_{-\theta/2} \cdot \mathbf{p} \end{bmatrix}, \quad (1)$$

for a Dirac electron at position \mathbf{r} , with linear momentum $\mathbf{p} = -i\hbar\nabla$ [7, 8, 29–32].

\mathcal{H} acts on four-component Dirac bispinors, related to the top and bottom graphene layers of the system, being respectively counter-clockwise rotated by $\theta/2$ and $-\theta/2$, along the out-of-plane axis z . The diagonal blocks in \mathcal{H} account for the isolated graphene sheets, of lattice constant $a = 2.46 \text{ \AA}$, lying parallel to the xy plane at distance d from each other. These terms involve the Cartesian Pauli matrices $\sigma_x, \sigma_y, \sigma_z$, through the rotated vector operators

$$\boldsymbol{\sigma}_{\pm\theta/2} = e^{-i(\pm\theta/4)\sigma_z} (\sigma_x, \sigma_y) e^{i(\pm\theta/4)\sigma_z}. \quad (2)$$

v_F denotes the group velocity at the corners (inequivalent K points) of the hexagonal first Brillouin zone (1stBZ) of graphene, where the Dirac-cone bands meet. The off-diagonal elements of \mathcal{H} express the interlayer coupling, dictated by the position-dependent hopping operator $\mathcal{T}(\mathbf{r})$, along with its hermitian conjugate $\mathcal{T}(\mathbf{r})^\dagger$.

By the spatial and time-reversal symmetry groups of TBG at low energies and small misalignment angles [30], the interlayer potential can be expanded into a Fourier series over the wave vectors that connect equivalent Dirac-cone vertices between the reciprocal sublattices of the top and bottom layers. The series is dominated by nearest-neighbor contributions from the rotated 1stBZ's of the two reciprocal sublattices, characterized by the center-to-corner distance $K_D = 4\pi/3a$.

Hereinafter, we use $\mathbf{a}_1 = a(1, \sqrt{3})/2$, $\mathbf{a}_2 = a(-1, \sqrt{3})/2$ as basis of real-space lattice vectors, and $\mathbf{b}_1 = 2\pi(1, 1/\sqrt{3})/a$, $\mathbf{b}_2 = 2\pi(-1, 1/\sqrt{3})/a$ as basis of reciprocal-space lattice vectors, for unrotated graphene. With this choice, reported in Fig. 1a, the leading terms in the Fourier expansion of $\mathcal{T}(\mathbf{r})$ are associated to the wave vectors $\mathbf{q}_1 = k_\theta(0, -1)$, $\mathbf{q}_2 = k_\theta(\sqrt{3}/2, 1/2)$ and $\mathbf{q}_3 = k_\theta(-\sqrt{3}/2, 1/2)$, of equal modulus $k_\theta = 2K_D \sin(\theta/2)$, which generate the reciprocal lattice of TBG, sketched in Fig. 1b. Accordingly, $\mathcal{T}(\mathbf{r})$ is approximated to the three-element sum

$$\mathcal{T}(\mathbf{r}) = \sum_{l=1}^3 T_l e^{i\mathbf{q}_l \cdot \mathbf{r}}, \quad (3)$$

whose Fourier coefficients

$$\begin{aligned} T_1 &= \omega_{AA}\sigma_0 + \omega_{AB}\sigma_x, \\ T_2 &= \omega_{AA}\sigma_0 - \frac{\omega_{AB}}{2} (\sigma_x - \sqrt{3}\sigma_y), \\ T_3 &= \omega_{AA}\sigma_0 - \frac{\omega_{AB}}{2} (\sigma_x + \sqrt{3}\sigma_y), \end{aligned} \quad (4)$$

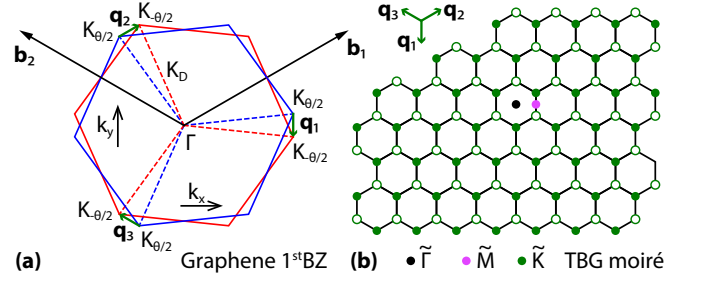


Figure 1. (a) Rotated 1stBZ's of the graphene sublattices in TBG. $K_{\pm\theta/2}$ denote the equivalent Dirac-cone vertices, connected by wave vectors \mathbf{q}_1 , \mathbf{q}_2 and \mathbf{q}_3 . K_D is the distance of the $K_{\pm\theta/2}$ points from the 1stBZ-center, or Γ point. \mathbf{b}_1 and \mathbf{b}_2 label the basis vectors for the unrotated reciprocal lattice of graphene. (b) Reciprocal space of TBG. \mathbf{q}_1 , \mathbf{q}_2 and \mathbf{q}_3 generate a triangular arrangement of equivalent \tilde{K} points, which, together with their inequivalent counterparts, make the periodically replicated 1stBZ of the moiré, with center $\tilde{\Gamma}$ and mid-point \tilde{M} .

depend on the Cartesian Pauli matrices, the 2×2 identity matrix σ_0 , plus two interlayer hopping energies, ω_{AA} and ω_{AB} , being respectively related to AA and AB (or BA) stacking centers [34].

Working under the limiting condition $\omega_{AA} = \omega_{AB} = \omega$, the interlayer Fourier coefficients of Eq. (4) become $T_l = \omega \tilde{T}_l$, and the reference Hamiltonian of Eq. (1) reduces to the Bistritzer-MacDonald (BM) Hamiltonian [7]. The latter establishes a minimal model capable of predicting the emergence of quasi-flat bands with vanishing group velocity at the Fermi level.

We now rely on the dimensionless position operator $\tilde{\mathbf{r}} = k_\theta \mathbf{r}$ and associated linear-momentum operator $\tilde{\mathbf{p}} = -i\nabla_{\tilde{\mathbf{r}}}$, which allow the BM Hamiltonian to be written as

$$\mathcal{H} = \begin{bmatrix} \hbar v_F k_\theta \boldsymbol{\sigma}_{\theta/2} \cdot \tilde{\mathbf{p}} & \omega \tilde{\mathcal{T}}(\tilde{\mathbf{r}}) \\ \omega \tilde{\mathcal{T}}(\tilde{\mathbf{r}})^\dagger & \hbar v_F k_\theta \boldsymbol{\sigma}_{-\theta/2} \cdot \tilde{\mathbf{p}} \end{bmatrix}. \quad (5)$$

Eq. (5) depends on the dimensionless hopping operator $\tilde{\mathcal{T}}(\tilde{\mathbf{r}})$, obtained by replacing T_l in Eq. (3) with the ω -independent Fourier coefficients \tilde{T}_l . Two characteristic energies are outlined. The Dirac-cone energy $\hbar v_F k_\theta$, associated to the (dimensionless) unperturbed Hamiltonian

$$\tilde{\mathcal{H}}_0 = \begin{bmatrix} \boldsymbol{\sigma}_{\theta/2} \cdot \tilde{\mathbf{p}} & 0 \\ 0 & \boldsymbol{\sigma}_{-\theta/2} \cdot \tilde{\mathbf{p}} \end{bmatrix}, \quad (6)$$

and the interlayer coupling energy ω , associated to the (dimensionless) perturbing potential

$$\tilde{\mathcal{H}}_T = \begin{bmatrix} 0 & \tilde{\mathcal{T}}(\tilde{\mathbf{r}}) \\ \tilde{\mathcal{T}}(\tilde{\mathbf{r}})^\dagger & 0 \end{bmatrix}. \quad (7)$$

The BM Hamiltonian may be thus reexpressed as

$$\mathcal{H} = \hbar k_\theta v_F \left(\tilde{\mathcal{H}}_0 + \gamma \tilde{\mathcal{H}}_T \right), \quad \gamma = \frac{\omega}{\hbar k_\theta v_F}. \quad (8)$$

Notably, this operator depends on the single parameter γ that controls the physics of the system. This implies that varying ω and θ , while keeping γ constant, leaves the eigenstates of \mathcal{H} unchanged, while the corresponding eigenvalues are scaled by the common factor $\hbar k_{\theta} v_F$.

Numerical calculations show the appearance of quasi-flat energy bands with vanishing Fermi velocity, for suitable choices of γ and ω . In particular, $\gamma=3^{-1/2}$ and $\omega=\omega_{\text{MA}}=0.11$ eV lead to a sequence of magic angles with maximum value $\theta_{\text{MA}}\sim 1.05^\circ$ [7].

Let us now denote by \mathcal{O}_{BM} the set of all Hamiltonians of the BM type given by Eq. (8), depending on ω and θ . Let us consider two generic elements $\mathcal{H}_1 = \mathcal{H}(\omega_1, \theta_1)$ and $\mathcal{H}_2 = \mathcal{H}(\omega_2, \theta_2)$ in \mathcal{O}_{BM} . We may introduce the equivalence relation

$$\mathcal{H}_1 \underset{\gamma}{\sim} \mathcal{H}_2 \iff \frac{\omega_1}{\hbar k_{\theta_1} v_F} = \frac{\omega_2}{\hbar k_{\theta_2} v_F} = \gamma \in \mathbb{R} \quad (9)$$

By doing so, we have partitioned \mathcal{O}_{BM} into infinite equivalence classes of the form

$$[\mathcal{H}]_{\gamma} \equiv \{\mathcal{H} \in \mathcal{O}_{\text{BM}} : \mathcal{H}_{\gamma} \underset{\gamma}{\sim} \mathcal{H}\}, \quad (10)$$

where \mathcal{H}_{γ} is a representative of the γ class. If \mathcal{H}_1 and \mathcal{H}_2 belong to $[\mathcal{H}]_{\gamma}$, then they have the same eigenstates and present *homothetic spectra*, which differ by a multiplication factor. In particular, the spectrum of \mathcal{H}_1 is obtained from the spectrum of \mathcal{H}_2 multiplied by

$$s_2^1 = \frac{k_{\theta_1}}{k_{\theta_2}} = \frac{\sin(\theta_1/2)}{\sin(\theta_2/2)}. \quad (11)$$

Among the different γ classes in \mathcal{O}_{BM} , we can identify a specific equivalent class, denoted γ_{MA} , for which a representative element is just one of the above outlined MA Hamiltonians, for example the one set by $\omega=\omega_{\text{MA}}$ and $\theta=\theta_{\text{MA}}$. Accordingly, all the Hamiltonians in $[\mathcal{H}]_{\gamma_{\text{MA}}}$ present an equal number of energy bands with vanishing group velocity at the Fermi level.

At this point, we use the fact that the interlayer hopping energy ω depends on the interlayer distance d [33, 35]. We may then assume that a bijective function F of d exist, being such that

$$\omega(d) = \omega(d_0)F(d), \quad (12)$$

where $F(d_0) = 1$ at a reference distance d_0 .

Let us consider a specific equivalence class γ , spanned by the representative twist angle θ_0 at the interlayer distance d_0 . By the defining relation (9) and the bijectivity of F , there exists a unique interlayer distance

$$d_{\gamma}(\theta) = F^{-1}\left(\frac{k_{\theta}}{k_{\theta_0}}\right), \quad (13)$$

for any other twist angle θ , which determines a BM Hamiltonian of the same class.

Let us now focus back on the equivalence class of MATBG, represented by the Hamiltonian $\mathcal{H}_{\gamma_{\text{MA}}}$ with geometric parameters θ_{MA} and ω_{MA} . We may set $\theta_0=\theta_{\text{MA}}$

and associate ω_{MA} to the well-known interlayer distance $d_0=3.349$ Å of bilayer graphene or graphite. Then, we can take any twist angle θ and its corresponding *magic* interlayer distance $d_{\gamma_{\text{MA}}}(\theta)$. These two parameters generate a BM Hamiltonian in $[\mathcal{H}]_{\gamma_{\text{MA}}}$, which hosts the same number of bands, with vanishing Fermi velocity, as the MATBG Hamiltonian. However, the tiny dispersive widths observed in the quasi-flat bands of MATBG on the meV scale, are amplified by the $k_{\theta}/k_{\theta_{\text{MA}}}$ factor, which may pose a limitation on the Hamiltonian of the γ_{MA} class with large stacking angles.

The construction carried out so far is valid at the CM level, within the limits outlined in appendix B. Inclusion of relaxation effects is possible by a straightforward redefinition of the Fourier coefficients \tilde{T}_l , as mentioned in appendix C. Nonetheless, d and θ are two experimental geometric parameters, which uniquely determine, up to symmetry operations, the configuration of a TBG. For this reason, it may be possible to construct an equivalence class for the electronic states near the Fermi level, regardless of the underlying theory.

Such a conjecture leads to two remarkable consequences. (i) In experiments involving TBG samples at small twist angles, the magic quasi-flat bands at the Fermi level should be achieved by tuning an external pressure, as reported in some previous studies [20–24]. (ii) The possibility to have quasi-flat bands at the Fermi level, in a TBG of twist angles relatively larger than the magic angle, may allow the characterization of MATBG, using an equivalent auxiliary system made of relatively small numbers of atoms per unit cell. While other scaling procedures with the same aim do exist [25–28] (see also Appendix A), connecting them to the defining parameters of TBG, the stacking angle and distance, may open to atomistic approaches, beyond the CM and TB approaches.

III. AN EQUIVALENCE RELATION FOR TIGHT-BINDING HAMILTONIANS

The present section is devoted to numerically assess the existence of the MATBG equivalence class, and derive a suitable functional form for Eq. (13). As a validation method, we employ a tight-binding approach, focusing on the electronic properties of TBG structures at different values of θ and d . The TB Hamiltonian takes the quadratic form

$$\mathcal{H} = \sum_i \epsilon_i c_i^{\dagger} c_i - \sum_{i \neq j} t_{ij} c_i^{\dagger} c_j, \quad (14)$$

expressed in terms of the creation operators c_i^{\dagger} , and annihilation operators c_i , for an electron with energy ϵ_i at the lattice site i . The t_{ij} matrix elements define the hopping amplitudes between lattice sites i and j , depending on their relative position vector \mathbf{r}_{ij} , of modulus r_{ij} and perpendicular component z_{ij} to the graphene sheets.

A minimal description of TBG is expressed in terms of p_z orbitals centered at the lattice sites [36], within the Slater-Koster (SK) formalism [37]. The on-site energies ϵ_i have the p -orbital symmetry. The hopping amplitudes are split into intralayer ($pp\pi$) and interlayer ($pp\sigma$) parts,

$$t_{ij} = n_{ij}^2 V_{pp\sigma}(r_{ij}) + (1 - n_{ij}^2) V_{pp\pi}(r_{ij}), \quad (15)$$

modulated by the out-of-plane directional cosines $n_{ij} = z_{ij}/r_{ij}$. The non-standard SK parameterization

$$V_{pp\pi}(r_{ij}) = -t_0 e^{-\delta(r_{ij}-a_c)} c(r_{ij}) \quad (16)$$

$$V_{pp\sigma}(r_{ij}) = t_1 e^{-\eta(d-d_0)} e^{-\delta(r_{ij}-d)} c(r_{ij}) \quad (17)$$

provides a reasonably accurate model, which accounts for structural deformation and out-of-plane atomic corrugation effects [24]. Here, $a_c = a/\sqrt{3} = 1.42 \text{ \AA}$ is the in-plane nearest-neighbor distance between two atomic sites. $d_0 = 3.349 \text{ \AA}$ labels the above-introduced equilibrium distance between the TBG planes, without applied pressure. $t_0 = 2.8 \text{ eV}$ and $t_1 = 0.44 \text{ eV}$ respectively denote the intralayer and interlayer hopping energies. $c(r) = (1 + e^{(r-r_c)/l_c})^{-1}$ is a smooth function in which $r_c = 0.265 \text{ \AA}$ and $l_c = 5.0 \text{ \AA}$. The ranges of $V_{pp\pi}$ and $V_{pp\sigma}$ are controlled by $\delta = 2.18 \text{ \AA}^{-1}$. Vertical compression effects are encompassed in $\eta = 0.58 \text{ \AA}^{-1}$.

TB calculations are performed using the TBPLas package [38], by retaining all the hoppings with $r_{ij} \lesssim 7.5 \text{ \AA}$. Using the standard SK parameterization [39], i.e., plugging $d = d_0$ in Eq. (17), the TB Hamiltonian presents four nearly flat bands with vanishing Fermi velocity at $\theta = 1.050^\circ$. This fact is reported in Fig. 2a and 2c, where the band structure of MATBG is plotted along the $\tilde{\Gamma}\tilde{K}\tilde{M}\tilde{\Gamma}$ border of the irreducible 1stBZ of the system, depicted in Fig. 1b.

To further simplify the treatment, we select TBG structures in which the mismatch angle between the two graphene layers leads to commensurate arrangements [8, 29, 40, 41]. In this specific scenario, using AA-stacked bilayer graphene as reference, the angle of mismatch between the two TBG layers reads

$$\cos(\theta_m) = \frac{3m^2 + 3m + 1/2}{3m^2 + 3m + 1}, \quad (18)$$

with m being an integer. Moving the coordinate system so that it aligns with the bottom graphene sheet, the moiré super-structure for commensurate TBG, with twist angle θ_m , is generated by the primitive vectors

$$\begin{bmatrix} \mathbf{t}_1(m) \\ \mathbf{t}_2(m) \end{bmatrix} = \begin{bmatrix} m & m+1 \\ -(m+1) & 2m+1 \end{bmatrix} \begin{bmatrix} \mathbf{a}_1 \\ \mathbf{a}_2 \end{bmatrix}. \quad (19)$$

The latter are obtained as linear combinations of the chosen basis vectors $\mathbf{a}_1, \mathbf{a}_2$ for unrotated graphene, see discussion in Sec. II and Fig. 1a.

As discussed above and shown in Fig. 2a, with the TB parameters at hand, the Hamiltonian of Eq. (14) satisfies the MA condition, at the geometric parameters

$\theta_{31} = 1.050^\circ$, obtained by letting $m = 31$ in Eq. (18), and $d_{31} = d_0$. The next step is constructing an equivalence class for this Hamiltonian. To do so, we have sorted the d parameter to different interlayer distances, at fixed twist angle θ_m . In the procedure, we have looked for a band structure hosting nearly non-dispersive band states at the Fermi level, which most closely resemble the MA bands when compressed by the scaling factor s_m^{31} , cfr. Eq. (11). We found a well-converged *magic distance* that fulfills this conditions, for each tested θ_m .

To better illustrate the process, we consider two random twist angles greater than θ_{31} , namely, $\theta_9 = 3.481^\circ$ and $\theta_{11} = 2.876^\circ$. The sorting procedure returns the magic distances $d_9 = 2.7329 \text{ \AA}$, for θ_9 , and $d_{11} = 2.8304 \text{ \AA}$, for θ_{11} . Let us inspect the energy spectra of the two TBG systems.

Fig. 2b reports the band structures obtained with θ_9 - d_9 (green lines) and θ_{11} - d_{11} (blue lines), which, at a rough look, appear to differ by an overall scaling factor. Furthermore, the MATBG spectrum in Fig. 2a is extraordinarily similar to the TBG spectra in Fig. 2b, over a different energy scale. We may then apply the scaling factors $s_9^{31} = k_{\theta_{31}}/k_{\theta_9} = 0.3017$ and $s_{11}^{31} = k_{\theta_{31}}/k_{\theta_{11}} = 0.3652$ to the bands in Fig. 2b, and compare them with the MATBG band system.

As shown in Fig. 2c, the scaled dispersions from the two TBG samples practically coincide with the MATBG dispersions in their low-energy parts, within $\sim 0.04 \text{ eV}$ around the Fermi level, which establishes the range of validity of the CM, see also appendix B. Strictly speaking, the equivalence class γ_{MA} is well-defined within this range. Nonetheless, we may extend the definition (9) at the TB level, by saying that two TB Hamiltonian are equivalent if their energy bands differ by an overall scaling factor in the CM limit.

We have thus reasonably proved that the low-energy spectra from TBG structures with θ_9 - d_9 and θ_{11} - d_{11} are both mapped onto the magic angle spectrum. As a further step towards the validation of the equivalence class, we look at the space distribution of the quasi-flat band states. In particular, we focus on the local electronic density, projected onto the quasi-flat-band range. Fig. 2d-f reports the projected density profiles for the three TBG systems, which appear to be strongly localized around the AA stacking regions of the corresponding moiré lattices, while they are practically vanishing in the AB stacking regions. This result is consistent with a number of previous studies [14, 33, 42–44]. More importantly, it allows us to conclude that the eigenstates corresponding to quasi-flat bands, in the same equivalence class, share the same localization properties.

The just outlined procedure was applied to a variety of TBG systems, with twist angles falling in the range of validity of the CM, see appendix B. In particular, Fig. 3 reports the interlayer magic distances d_M for which nearly non-dispersive bands were obtained as function of the twist angle θ , in the range of $\theta_{31} = 1.050^\circ$ to $\theta_5 = 6.009^\circ$. As already pointed out, the main effect of reducing the

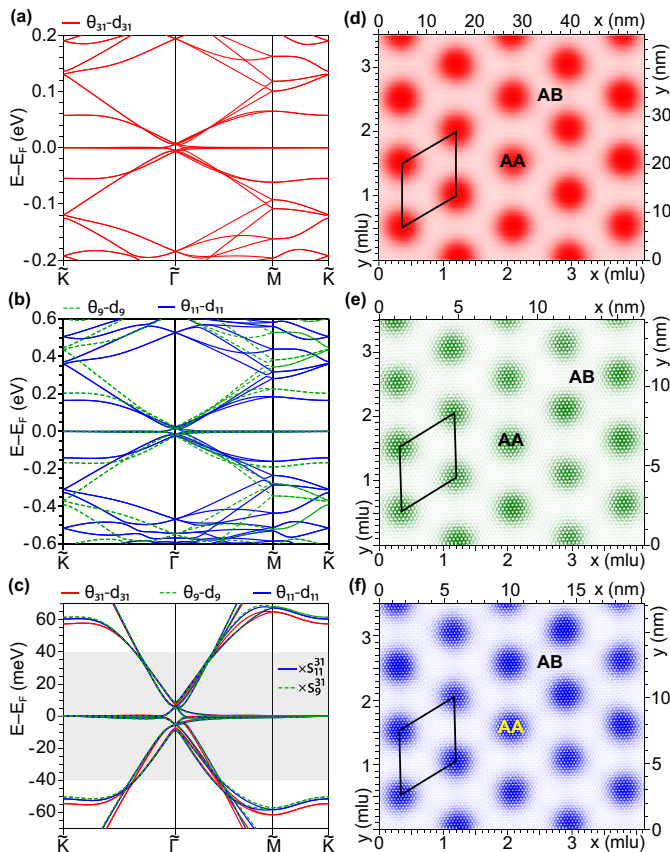


Figure 2. (a) Band structure of MATBG, as obtained with the geometric parameters $\theta_{31}=1.050^\circ$ and $d_{31} = 3.349 \text{ \AA}$, within the TB approach illustrated in the main text. (b) Band dispersions of two TBG structures with $\theta_9=3.481^\circ$ and $d_9=2.7329 \text{ \AA}$ (green lines), $\theta_{11}=2.876^\circ$ and $d_{11}=2.8304 \text{ \AA}$ (blue lines). (c) Compressed band dispersions of panel (b), obtained with the scaling factors $s_9^{31} = 0.3017$ (green), $s_{11}^{31} = 0.3652$ (blue), and superimposed to the MATBG bands (red). The three spectra, reported against the $\tilde{\Gamma}\tilde{K}\tilde{M}\tilde{\Gamma}$ contour of the moiré 1stBZ, shown in Fig. 1b, coincide within $\sim 0.04 \text{ eV}$ around the Fermi level (gray shaded area). (d)-(f) Projected local density at the Fermi level of (d) MATBG, (e) TBG with θ_9-d_9 , and (f) TBG with $\theta_{11}-d_{11}$, calculated by applying the TB propagation method. The in-plane coordinates are provided both in nm and moiré lattice units (mlu). The black parallelograms denote the moiré unit cells of the three TBG systems. Density peaks occur around the AA stacking regions, while density dips characterize the AB stacking regions.

distance between the TBG layers is to modify the inter-layer interaction. In the TB approach, this results in a variation of the interlayer hopping integral. Turning to the CM limit, we want to derive a smooth and bijective dependence of the hopping parameter ω on the interlayer distance d , thus providing an explicit expression to the F function in Eq. (12). We may assume the simple exponential scaling law

$$\omega(d) = \omega(d_0)e^{-\beta(d-d_0)}, \quad d \geq d_0, \quad (20)$$

parametrized in terms of the inverse damping length

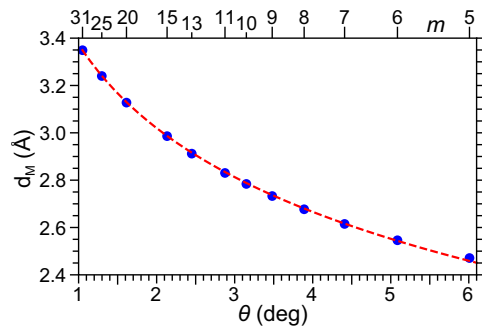


Figure 3. Magic distance d_M vs stacking angle θ , as obtained through the TB method of the main text. Also reported on the top horizontal axis are the values of m , cfr. Eq. (18). The red dashed line corresponds to the merit function of Eq. (21), with the best-fit parameter $\beta = 1.957 \text{ \AA}^{-1}$.

β . Then, placing ourselves in the equivalence class of MATBG, we obtain that the data of Fig. 3 are correlated by the following merit function

$$d_M(\theta) = d_0 - \frac{1}{\beta} \ln \left[\frac{\sin(\theta/2)}{\sin(\theta_0/2)} \right], \quad (21)$$

with $d_0 = d_{31}$ and $\theta_0 = \theta_{31}$. Eq. (21) is indeed in excellent agreement with the data at the best-fit value $\beta = 1.957 \text{ \AA}^{-1}$, as also reported in Fig. 3.

We have thus provided reasonable arguments that an equivalence class for the MA condition exists and is well-defined at the TB level.

IV. EQUIVALENCE-CLASS APPROACH AND DFT

We now apply the equivalence class concept to DFT, suggesting how the low-energy features of some selected TBG systems, arranged in the commensurate lattices, set by Eqs. (18) and (19), can be linked to the MA condition. DFT calculations were run using the Quantum Espresso (QE) package [45, 46], within the projector augmented wave (PAW) method [47] provided by the PseudoDojo PAW datasets [48]. The Perdew-Burke-Ernzerhof (PBE) exchange-correlation functional [49] was adopted, in conjunction with a plane-wave cutoff of 30 Ry, and an energy convergence criterion of 10^{-6} Ry for the self-consistent runs. The TBG slab was given an out-of-plane vacuum region of 20 \AA . The 1stBZ was sampled over Monkhorst-Pack grids [50] of 2×2 to 6×6 points, equivalent to average spacings between 0.0004 \AA^{-1} and 0.007 \AA^{-1} . A Marzari-Vanderbilt smearing function [51] of 0.01 Ry in width was included, to fasten convergence.

We focused on three specific stacking angles, namely, $\theta_5=6.009^\circ$, $\theta_6=5.086^\circ$ and $\theta_7=4.408^\circ$, being sufficiently larger than the magic angle, while falling around the range of applicability of the CM model. Then, we adopted a similar sorting procedure as the TB method,

that is, we carried out several DFT calculations by varying the interlayer distance until nearly non-dispersive KS bands at the Fermi level were detected. The DFT search returned the magic distances $\tilde{d}_5=2.450$ Å, $\tilde{d}_6=2.540$ Å and $\tilde{d}_7=2.616$ Å, which gave the least dispersive band dispersions at the Fermi level, within numerical uncertainties below 0.05 Å. Interestingly, the TB predictions for the magic distances are $d_5=2.470$ Å, $d_6=2.546$ Å and $d_7=2.615$ Å, as extracted from Fig. 3 with the same stacking angles. This very good agreement suggests using the TB magic distances as a starting guess to speed up the DFT search process.

In Fig. 4, we report the DFT spectra obtained with θ_5 - \tilde{d}_5 , θ_6 - \tilde{d}_6 and θ_7 - \tilde{d}_7 by respectively processing 364, 508 and 676 atoms per unit-cell. Looking at Fig. 4a-c, we see the main features of the band structure, given by the presence of four nearly flat bands around the Fermi level, with vanishing group velocity at the corners of the moiré 1stBZ, namely the \bar{K} points and their inequivalent counterparts shown in Fig. 1b. For the angle θ_5 , even though we manage to extract a suitable magic distance, the four flat bands, compressed by s_5^{31} , exhibit a greater bandwidth as compared to the θ_6 - \tilde{d}_6 and θ_7 - \tilde{d}_7 cases. A wider bandwidth was also detected at the TB level, which demonstrates that $\theta \sim 6^\circ$ is the upper limit of applicability of our results. In Fig. 4d-f, we show the local electron density, projected onto the quasi-non-dispersive states, in the range of -0.05 eV to 0.05 eV, around the Fermi energy. This quantity shows that the wave functions of the four bands are strongly localized in the AA stacking regions.

We should also point out that, due to the large unit cell size of the magic-angle twisted bilayer graphene, we do not have direct access to its fundamental ground-state properties, through DFT. Indeed, the twist angle θ_{31} produces a commensurate TBG lattice with 11908 atoms per unit cell. An atomistic self-consistent computation for such a system would be unfeasible even by largest, currently available, high-performance computing resources. Furthermore, it is not guaranteed that the MA condition is fulfilled for the $\theta_{31} \sim 1.050^\circ$ value, at the DFT level. Therefore, the θ_7 - \tilde{d}_7 , θ_6 - \tilde{d}_6 and θ_5 - \tilde{d}_5 conditions may not precisely fall in the same equivalence class of MATBG. However, they both share with MATBG the two main features, that is four nearly flat bands at the Fermi level with vanishing group velocity at the 1stBZ corners, and eigenfunctions strongly localized in the AA stacking region of the moiré lattice. In addition, the agreement of TB and DFT approaches on the magic distances, suggests that the inaccessible MA spectrum of DFT at θ_{31} may be close to the ones obtained by applying the TB compression factors $s_7^{31}=0.2383$, $s_6^{31}=0.2065$ and $s_5^{31}=0.1748$ to our DFT spectra. The compressed DFT band structures of TBG, for the θ_7 - \tilde{d}_7 , θ_6 - \tilde{d}_6 and θ_5 - \tilde{d}_5 cases, can be respectively read from Fig. 4a-c, by looking at the secondary vertical axis with red ticks. The three scaled spectra show very similar dispersions within 100 meV around the Fermi level, however, they should present identical

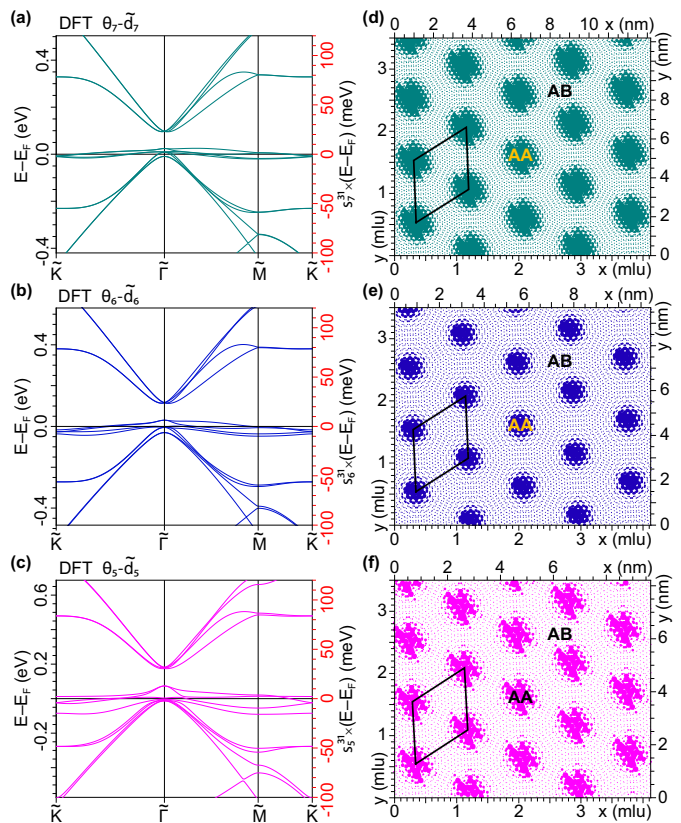


Figure 4. (a)-(c) DFT band structure of a TBG with the geometric parameters (a) $\theta_7=4.408^\circ$ - $\tilde{d}_7=2.616$ Å, (b) $\theta_6=5.086^\circ$ - $\tilde{d}_6=2.540$ Å and (c) $\theta_5=6.009^\circ$ - $\tilde{d}_5=2.450$ Å. The energy ticks in the secondary vertical axis (red) are scaled to the width of the MATBG energy spectrum of Fig. 2a, by (a) $s_7^{31}=0.2383$, (b) $s_6^{31}=0.2065$ and (c) $s_5^{31}=0.1748$. (d)-(f) Localized density associated to the four quasi-flat bands for (d) θ_7 - \tilde{d}_7 , (e) θ_6 - \tilde{d}_6 and (f) θ_5 - \tilde{d}_5 , near charge neutrality. All other settings are as in Fig. 2.

features. We here interpret these differences as a measure of error in finding the DFT features of MATBG by the equivalent class approach. We may accordingly infer that the three considered TBG systems are in a *nearby* equivalence class to that of MATBG, being characterized by the interaction parameter $\gamma=\gamma_{\text{MA}}+\delta\gamma$, in the CM, with $\delta\gamma/\gamma_{\text{MA}} \ll 1$.

To further support this statement, in Fig. 5, we compare the results for MATBG, as obtained with the TB approach outlined in Sec. III, and the above discussed θ_7 - \tilde{d}_7 and θ_6 - \tilde{d}_6 cases, along with compression factors s_7^{31} and s_6^{31} . We see that the two DFT compressed spectra are practically overlapping, see Fig. 5a-c, within an error window of less than ~ 5 meV, which occurs in the quasi-flat band region, see Fig. 5c.

In addition, the DFT and TB occupied dispersive levels are also very close to one another, see Fig. 5a. Similar conclusions can be raised on the unoccupied dispersive parts of the spectra, given in Fig. 5b, apart from a global shift of about 20 meV. The DFT and TB quasi-

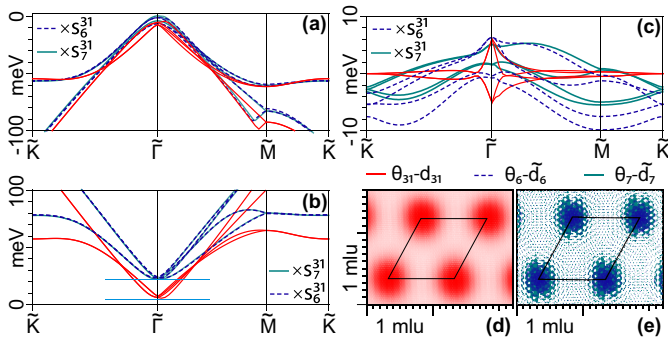


Figure 5. (a)-(c) DFT band structure of TBG, with geometric parameters $\theta_6\text{-}\tilde{d}_6$, $\theta_7\text{-}\tilde{d}_7$, and compression factors s_6^{31} , s_7^{31} , vs. TB band structure of MATBG. (a) Occupied dispersive levels, (b) unoccupied dispersive levels, (c) quasi-flat bands. (d), (e) Projected electron density onto the quasi-flat band states for (d) MATBG and (e) TBG structures of (a)-(c).

flat bands, on the other hand, appear to have rather different behaviors, see Fig. 5c. Nonetheless, the tiny dispersive ranges of these bands present similar widths, namely, ~ 16 meV with $\theta_6\text{-}\tilde{d}_6$ and ~ 10 meV with either MATBG or $\theta_7\text{-}\tilde{d}_7$. In addition, the projected electron densities onto these bands display consistent peaks and dips, when reported on the same moiré-lattice-unit scale, see Fig. 5c,e. We also need to point out that TB is a parametric approach, adjusted to experiments or consolidated theory, whereas DFT is an ab initio approach. Thus, the recorded differences between the two methods cannot be surprising. Indeed, TB and DFT calculations present even more marked differences when applied to known systems, such as graphene, leading to 15-20 % inaccuracies in the estimate of the Fermi velocity [52] and unoccupied band levels [53].

V. DISCUSSION

The significance of elucidating the existence of an equivalence class lies in the fact that MATBG, due to its very large moiré unit cell, represents a computationally inaccessible system, even to its ground state properties, when ab initio type methods are employed. The existence of equivalence classes, and the MATBG equivalence class in particular, may open the way to computations of ground-state and excited-state features, using more convenient geometric structures that are computationally affordable.

As a paradigmatic example, we suggest concentrating on the dynamical density-density response function of the TBG electrons around the quasi-flat band region [54]. The latter can be put in a form that depends on the DFT energies and wavefunctions of the system, plus, the electronic temperature embedded in the Fermi-Dirac distribution. At least in the random phase approximation (RPA), the interaction can be reduced to a smooth Coulomb-like form. By the equivalence-

class approach developed here, it may be possible to map one density-density response function onto another for structures belonging to the same equivalence class of MATBG, by carrying out TDDFT computations in moiré lattice units and suitably adjusting temperature, poles, and amplitudes using overall scaling factors similar to s_2^1 of Eq. (11). Following preliminary calculations to be run at the CM and/or TB levels, we may thus explore the nature of plasmon excitations in MATBG, setting up a computationally accessible strategy on an auxiliary TBG system, with a more convenient geometry. Indeed, a systematic study of light-trapping mechanisms related to plasmonic effects in this area is still lacking. Recent experimental studies seem to rule out a purely electronic coupling [55, 56], whereas, from a theoretical point of view, it has been proposed that collective excitations play a crucial role in the emergence of unconventional superconductivity phenomena [57–59].

Building upon the same considerations, it might be further possible to investigate the superconducting-normal state transition of a TBG with quasi-flat bands at a specific magic distance. In this case, the critical temperature should be re-normalized with a suitable scaling law, because we expect that critical temperature increases with increasing the stacking angle.

We finally observe that results discussed here are not limited to TBG. An equivalence relation could be defined on other twisted materials, made of two or multiple atomic layers that host Dirac-cone states in their isolated phases. Indeed, the weak interlayer interaction should always lead, under suitable limiting conditions, to a reference Hamiltonian of the BM type, which should be expressed in a form similar to Eq. (8). A crucial point of the treatment, particularly challenging in heterogeneous multilayer structures, would be to construct a smooth, bijective function of the hopping parameters to the interlayer distances.

VI. CONCLUSION

In conclusion, we have made explicit that MATBG belongs to a specific equivalence class, being well-defined in the framework of a continuum theory. All TBG structures of this class are generated by the twist angle and a *magic* interlayer distance. They exhibit homothetic spectra, fixed number of bands with vanishing Fermi velocity, and a common basis of eigenstates, which can be one-to-one mapped to MATBG through a dimensionless scaling factor associated to the twist angle. The equivalence relation can be extended to tight-binding models, by running a search algorithm on the interlayer distance at fixed twist angle, until the best homothetic match in the quasi-flat bands of the selected TBG with those of MATBG is found. Restricting our observations to commensurate lattices, we have identified a one-to-one smooth correspondence between TBG structures with twist angles below $\sim 6^\circ$ and MATBG. Next, we have analyzed the

DFT ground-state of superimposed graphene monolayers, twisted over the same limited angular range. We have set up an ab initio procedure to determine the optimal interlayer distance, for each tested case, which leads to quasi-flat bands with vanishing group velocity at the Fermi level. Finally, we have forced the validity of the equivalent-class concept to tentatively reconstruct the inaccessible DFT spectrum of MATBG. Our results may open the possibility to study, by using costly ab initio techniques, the electronic properties of systems with affordable numbers of atoms per unit cell, but with magic-angle-like properties. Additionally, they may guide the *experimental mapping* of a TBG system onto MATBG by suggesting the correct magic distance to be achieved

in compressing the system with an external pressure.

VII. ACKNOWLEDGEMENTS

We thank N. Lo Gullo, J. Settino, and F. Plastina for useful discussion. This research was partially supported *Centro Nazionale di Ricerca in High-Performance Computing, Big Data and Quantum Computing*, PNRR 4 2 1.4, CI CN00000013, CUP H23C22000360005. We acknowledge the *Marconi, Marconi100, Galileo100 and Leonardo* high performance computing resources, provided by the [CINECA consortium \(Italy\)](#), within the INF16_npqcd project, under the [CINECA-INFN](#) agreement. We also acknowledge the *Newton* high performance computing cluster, provided by the University of Calabria.

-
- [1] Y. Cao, V. Fatemi, S. Fang, K. Watanabe, T. Taniguchi, E. Kaxiras, and P. Jarillo-Herrero, Unconventional superconductivity in magic-angle graphene superlattices, [Nature](#) **556**, 43 (2018).
 - [2] Y. Cao, V. Fatemi, A. Demir, S. Fang, S. L. Tomarken, J. Y. Luo, J. D. Sanchez-Yamagishi, K. Watanabe, T. Taniguchi, E. Kaxiras, *et al.*, Correlated insulator behaviour at half-filling in magic-angle graphene superlattices, [Nature](#) **556**, 80 (2018).
 - [3] M. Yankowitz, S. Chen, H. Polshyn, Y. Zhang, K. Watanabe, T. Taniguchi, D. Graf, A. F. Young, and C. R. Dean, Tuning superconductivity in twisted bilayer graphene, [Science](#) **363**, 1059 (2019).
 - [4] X. Lu, P. Stepanov, W. Yang, M. Xie, M. A. Aamir, I. Das, C. Urgell, K. Watanabe, T. Taniguchi, G. Zhang, *et al.*, Superconductors, orbital magnets and correlated states in magic-angle bilayer graphene, [Nature](#) **574**, 653 (2019).
 - [5] A. L. Sharpe, E. J. Fox, A. W. Barnard, J. Finney, K. Watanabe, T. Taniguchi, M. Kastner, and D. Goldhaber-Gordon, Emergent ferromagnetism near three-quarters filling in twisted bilayer graphene, [Science](#) **365**, 605 (2019).
 - [6] J. M. Park, Y. Cao, K. Watanabe, T. Taniguchi, and P. Jarillo-Herrero, Flavour Hund's coupling, chern gaps and charge diffusivity in moiré graphene, [Nature](#) **592**, 43–48 (2021).
 - [7] R. Bistritzer and A. H. MacDonald, Moiré bands in twisted double-layer graphene, [Proceedings of the National Academy of Sciences](#) **108**, 12233 (2011).
 - [8] J. M. B. Lopes dos Santos, N. M. R. Peres, and A. H. Castro Neto, Continuum model of the twisted graphene bilayer, [Phys. Rev. B](#) **86**, 155449 (2012).
 - [9] E. Suárez Morell, J. D. Correa, P. Vargas, M. Pacheco, and Z. Barticevic, Flat bands in slightly twisted bilayer graphene: Tight-binding calculations, [Phys. Rev. B](#) **82**, 121407 (2010).
 - [10] M. Rosendo López, F. Peñaranda, J. Christensen, and P. San-Jose, Flat bands in magic-angle vibrating plates, [Phys. Rev. Lett.](#) **125**, 214301 (2020).
 - [11] Y. Xie, B. Lian, B. Jäck, X. Liu, C.-L. Chiu, K. Watanabe, T. Taniguchi, B. A. Bernevig, and A. Yazdani, Spectroscopic signatures of many-body correlations in magic-angle twisted bilayer graphene, [Nature](#) **572**, 101 (2019).
 - [12] A. Kerelsky, L. J. McGilly, D. M. Kennes, L. Xian, M. Yankowitz, S. Chen, K. Watanabe, T. Taniguchi, J. Hone, C. Dean, *et al.*, Maximized electron interactions at the magic angle in twisted bilayer graphene, [Nature](#) **572**, 95 (2019).
 - [13] Y. Jiang, X. Lai, K. Watanabe, T. Taniguchi, K. Haule, J. Mao, and E. Y. Andrei, Charge order and broken rotational symmetry in magic-angle twisted bilayer graphene, [Nature](#) **573**, 91 (2019).
 - [14] G. Li, A. Luican, J. Lopes dos Santos, A. Castro Neto, A. Reina, J. Kong, and E. Andrei, Observation of van Hove singularities in twisted graphene layers, [Nature physics](#) **6**, 109 (2010).
 - [15] Y. Choi, J. Kemmer, Y. Peng, A. Thomson, H. Arora, R. Polski, Y. Zhang, H. Ren, J. Alicea, G. Refael, *et al.*, Electronic correlations in twisted bilayer graphene near the magic angle, [Nature physics](#) **15**, 1174 (2019).
 - [16] S. Lisi, X. Lu, T. Benschop, T. A. de Jong, P. Stepanov, J. R. Duran, F. Margot, I. Cucchi, E. Cappelli, A. Hunter, *et al.*, Observation of flat bands in twisted bilayer graphene, [Nature Physics](#) **17**, 189 (2021).
 - [17] S. Carr, D. Massatt, S. Fang, P. Cazeaux, M. Luskin, and E. Kaxiras, Twistronics: Manipulating the electronic properties of two-dimensional layered structures through their twist angle, [Phys. Rev. B](#) **95**, 075420 (2017).
 - [18] G. Elizabeth, How magic angle graphene is stirring up physics, [Nature](#) **565**, 15 (2019).
 - [19] A. K. Geim and I. V. Grigorieva, Van der waals heterostructures, [Nature](#) **499**, 419 (2013).
 - [20] B. L. Chittari, N. Leconte, S. Javvaji, and J. Jung, Pressure induced compression of flatbands in twisted bilayer graphene, [Electronic Structure](#) **1**, 015001 (2018).
 - [21] F. Yndurain, Pressure-induced magnetism in rotated graphene bilayers, [Phys. Rev. B](#) **99**, 045423 (2019).
 - [22] S. Carr, S. Fang, P. Jarillo-Herrero, and E. Kaxiras, Pressure dependence of the magic twist angle in graphene superlattices, [Phys. Rev. B](#) **98**, 085144 (2018).

- [23] L. Ge, K. Ni, X. Wu, Z. Fu, Y. Lu, and Y. Zhu, Emerging flat bands in large-angle twisted bi-layer graphene under pressure, *Nanoscale* **13**, 9264 (2021).
- [24] X. Lin, H. Zhu, and J. Ni, Pressure-induced gap modulation and topological transitions in twisted bilayer and twisted double bilayer graphene, *Phys. Rev. B* **101**, 155405 (2020).
- [25] H. Sainz-Cruz, T. Cea, P. A. Pantaleón, and F. Guinea, High transmission in twisted bilayer graphene with angle disorder, *Phys. Rev. B* **104**, 075144 (2021).
- [26] J. Vahedi, R. Peters, A. Missaoui, A. Honecker, and G. T. de Laissardière, Magnetism of magic-angle twisted bilayer graphene, *SciPost Phys.* **11**, 083 (2021).
- [27] L. A. Gonzalez-Arraga, J. L. Lado, F. Guinea, and P. San-Jose, Electrically controllable magnetism in twisted bilayer graphene, *Phys. Rev. Lett.* **119**, 107201 (2017).
- [28] E. Andrade, P. A. Pantaleón, F. Guinea, and G. G. Naumis, Flat bands and electronic localization in twisted bilayer graphene nanoribbons, *Phys. Rev. B* **108**, 235418 (2023).
- [29] J. M. B. Lopes dos Santos, N. M. R. Peres, and A. H. Castro Neto, Graphene bilayer with a twist: Electronic structure, *Phys. Rev. Lett.* **99**, 256802 (2007).
- [30] L. Balents, General continuum model for twisted bilayer graphene and arbitrary smooth deformations, *SciPost Phys.* **7**, 048 (2019).
- [31] S. Carr, S. Fang, Z. Zhu, and E. Kaxiras, Exact continuum model for low-energy electronic states of twisted bilayer graphene, *Phys. Rev. Res.* **1**, 013001 (2019).
- [32] G. Tarnopolsky, A. J. Kruchkov, and A. Vishwanath, Origin of magic angles in twisted bilayer graphene, *Phys. Rev. Lett.* **122**, 106405 (2019).
- [33] G. Trambly de Laissardière, D. Mayou, and L. Magaud, Numerical studies of confined states in rotated bilayers of graphene, *Phys. Rev. B* **86**, 125413 (2012).
- [34] B. A. Bernevig, Z.-D. Song, N. Regnault, and B. Lian, Twisted bilayer graphene. iii. interacting hamiltonian and exact symmetries, *Phys. Rev. B* **103**, 205413 (2021).
- [35] R. Bistritzer and A. H. MacDonald, Transport between twisted graphene layers, *Phys. Rev. B* **81**, 245412 (2010).
- [36] X. Lin and D. Tománek, Minimum model for the electronic structure of twisted bilayer graphene and related structures, *Phys. Rev. B* **98**, 081410 (2018).
- [37] J. C. Slater and G. F. Koster, Simplified lcao method for the periodic potential problem, *Phys. Rev.* **94**, 1498 (1954).
- [38] Y. Li, Z. Zhan, X. Kuang, Y. Li, and S. Yuan, Tbpplas: A tight-binding package for large-scale simulation, *Computer Physics Communications* **285**, 108632 (2023).
- [39] H. Shi, Z. Zhan, Z. Qi, K. Huang, E. v. Veen, J. A. Silva-Guillén, R. Zhang, P. Li, K. Xie, H. Ji, M. I. Katsnelson, S. Yuan, S. Qin, and Z. Zhang, Large-area, periodic, and tunable intrinsic pseudo-magnetic fields in low-angle twisted bilayer graphene, *Nature Communications* **11**, 371 (2020).
- [40] E. J. Mele, Commensuration and interlayer coherence in twisted bilayer graphene, *Phys. Rev. B* **81**, 161405 (2010).
- [41] S. Shallcross, S. Sharma, E. Kandelaki, and O. A. Pankratov, Electronic structure of turbostratic graphene, *Phys. Rev. B* **81**, 165105 (2010).
- [42] K. Kim, A. DaSilva, S. Huang, B. Fallahazad, S. Larentis, T. Taniguchi, K. Watanabe, B. J. LeRoy, A. H. MacDonald, and E. Tutuc, Tunable moiré bands and strong correlations in small-twist-angle bilayer graphene, *Proceedings of the National Academy of Sciences* **114**, 3364 (2017).
- [43] I. Brihuega, P. Mallet, H. González-Herrero, G. Trambly de Laissardière, M. M. Ugeda, L. Magaud, J. M. Gómez-Rodríguez, F. Ynduráin, and J.-Y. Veullen, Unraveling the intrinsic and robust nature of van hove singularities in twisted bilayer graphene by scanning tunneling microscopy and theoretical analysis, *Phys. Rev. Lett.* **109**, 196802 (2012).
- [44] L.-H. Tong, Q. Tong, L.-Z. Yang, Y.-Y. Zhou, Q. Wu, Y. Tian, L. Zhang, L. Zhang, Z. Qin, and L.-J. Yin, Spectroscopic visualization of flat bands in magic-angle twisted monolayer-bilayer graphene: Coexistence of localization and delocalization, *Phys. Rev. Lett.* **128**, 126401 (2022).
- [45] P. Giannozzi, S. Baroni, N. Bonini, M. Calandra, R. Car, C. Cavazzoni, D. Ceresoli, G. L. Chiarotti, M. Cococcioni, I. Dabo, A. D. Corso, S. de Gironcoli, S. Fabris, G. Fratesi, R. Gebauer, U. Gerstmann, C. Gougoussis, A. Kokalj, M. Lazzeri, L. Martin-Samos, N. Marzari, F. Mauri, R. Mazzarello, S. Paolini, A. Pasquarello, L. Paulatto, C. Sbraccia, S. Scandolo, G. Sclauzero, A. P. Seitsonen, A. Smogunov, P. Umari, and R. M. Wentzcovitch, Quantum espresso: a modular and open-source software project for quantum simulations of materials, *Journal of Physics: Condensed Matter* **21**, 395502 (2009).
- [46] P. Giannozzi, O. Andreussi, T. Brumme, O. Bunau, M. B. Nardelli, M. Calandra, R. Car, C. Cavazzoni, D. Ceresoli, M. Cococcioni, N. Colonna, I. Carnimeo, A. D. Corso, S. de Gironcoli, P. Delugas, R. A. DiStasio, A. Ferretti, A. Floris, G. Fratesi, G. Fugallo, R. Gebauer, U. Gerstmann, F. Giustino, T. Gorni, J. Jia, M. Kawamura, H.-Y. Ko, A. Kokalj, E. Küçükbenli, M. Lazzeri, M. Marsili, N. Marzari, F. Mauri, N. L. Nguyen, H.-V. Nguyen, A. O. de-la Roza, L. Paulatto, S. Poncé, D. Rocca, R. Sabatini, B. Santra, M. Schlipf, A. P. Seitsonen, A. Smogunov, I. Timrov, T. Thonhauser, P. Umari, N. Vast, X. Wu, and S. Baroni, Advanced capabilities for materials modelling with quantum espresso, *Journal of Physics: Condensed Matter* **29**, 465901 (2017).
- [47] P. E. Blöchl, Projector augmented-wave method, *Phys. Rev. B* **50**, 17953 (1994).
- [48] F. Jollet, M. Torrent, and N. Holzwarth, Generation of Projector Augmented-Wave atomic data: A 71 element validated table in the XML format, *Comput. Phys. Commun.* **185**, 1246 (2014).
- [49] J. P. Perdew, K. Burke, and M. Ernzerhof, Generalized gradient approximation made simple, *Phys. Rev. Lett.* **77**, 3865 (1996).
- [50] H. J. Monkhorst and J. D. Pack, Special points for brillouin-zone integrations, *Phys. Rev. B* **13**, 5188 (1976).
- [51] N. Marzari, D. Vanderbilt, A. De Vita, and M. C. Payne, Thermal contraction and disordering of the al(110) surface, *Phys. Rev. Lett.* **82**, 3296 (1999).
- [52] P. E. Trevisanutto, C. Giorgetti, L. Reining, M. Ladisa, and V. Olevano, Ab initio *gw* many-body effects in graphene, *Phys. Rev. Lett.* **101**, 226405 (2008).
- [53] A. Sindona, M. Pisarra, C. Vacacela Gomez, P. Riccardi, G. Falcone, and S. Bellucci, Calibration of the fine-structure constant of graphene by time-dependent density-functional theory, *Phys. Rev. B* **96**, 201408 (2017).

- [54] G. F. Giuliani and G. Vignale, *Quantum theory of the electron liquid* (Cambridge Univ. Press, Cambridge, 2005).
- [55] P. Stepanov, I. Das, X. Lu, A. Fahimniya, K. Watanabe, T. Taniguchi, F. H. Koppens, J. Lischner, L. Levitov, and D. K. Efetov, Untying the insulating and superconducting orders in magic-angle graphene, *Nature* **583**, 375 (2020).
- [56] J. Ge, Y. Saito, T. Taniguchi, K. Watanabe, and A. Young, Independent superconductors and correlated insulators in twisted bilayer graphene, in *APS March Meeting Abstracts* (2021) pp. R42–005.
- [57] G. Sharma, M. Trushin, O. P. Sushkov, G. Vignale, and S. Adam, Superconductivity from collective excitations in magic-angle twisted bilayer graphene, *Phys. Rev. Res.* **2**, 022040 (2020).
- [58] L. Peng, I. Yudhistira, G. Vignale, and S. Adam, Theoretical determination of the effect of a screening gate on plasmon-induced superconductivity in twisted bilayer graphene (2023), [arXiv:2309.14767 \[cond-mat.supr-con\]](https://arxiv.org/abs/2309.14767).
- [59] T. Cea and F. Guinea, Coulomb interaction, phonons, and superconductivity in twisted bilayer graphene, *Proceedings of the National Academy of Sciences* **118**, e2107874118 (2021).
- [60] K. Uchida, S. Furuya, J.-I. Iwata, and A. Oshiyama, Atomic corrugation and electron localization due to moiré patterns in twisted bilayer graphenes, *Phys. Rev. B* **90**, 155451 (2014).
- [61] M. M. van Wijk, A. Schuring, M. I. Katsnelson, and A. Fasolino, Relaxation of moiré patterns for slightly misaligned identical lattices: graphene on graphite, *2D Materials* **2**, 034010 (2015).
- [62] S. Dai, Y. Xiang, and D. J. Srolovitz, Twisted bilayer graphene: Moiré with a twist, *Nano Letters* **16**, 5923 (2016).
- [63] N. N. T. Nam and M. Koshino, Lattice relaxation and energy band modulation in twisted bilayer graphene, *Phys. Rev. B* **96**, 075311 (2017).
- [64] M. Koshino, N. F. Q. Yuan, T. Koretsune, M. Ochi, K. Kuroki, and L. Fu, Maximally localized wannier orbitals and the extended hubbard model for twisted bilayer graphene, *Phys. Rev. X* **8**, 031087 (2018).

Appendix A: Alternative equivalence relations for tight-binding Hamiltonians

In the main text, we put much effort in defining an equivalence relation for MATBG by varying the interlayer distance. In particular, the TB calculations presented in Sec. III were based on a Slater-Koster parametrization of the interlayer hopping potential $V_{pp\sigma}$, cfr. Eq. (17), which allowed us to operate on the d parameter of the compression factor $e^{-\eta(d-d_0)}$. By doing so, we established a search algorithm to achieve homothetic, nearly non-dispersive states, being equivalent to those of the MATBG at angles greater than θ_{MA} .

Given the equivalence relation of Eq. (9), we may explore alternative approaches to derive Hamiltonians of the same equivalence class at the TB level, by modifying the interlayer hopping in Eq. (15). For example, we can adopt the following parametrization

$$V_{pp\sigma}(r_{ij}) = t_1 \frac{\sin(\theta/2)}{\sin(\theta_{\text{MA}}/2)} e^{\delta(d_0-r_{ij})} c(r_{ij}), \quad (\text{A1})$$

holding close to the magic angle, which corresponds to replace $e^{-\eta(d-d_0)}$ in Eq. (17) with the scaling factor that sets the equivalence relation of MATBG, cfr. Eq. (11). Accordingly, we can operate on θ_{MA} at constant d_0 to find an optimal magic value, associated to θ , which establishes the equivalence relation for the corresponding TBG Hamiltonian. In other words, we can *move* within the equivalence class of MATBG at constant interlayer distance and look for a renormalized magic angle $\hat{\theta}_M$ to build up the equivalence relation.

Further scaling procedures are available by modifying the other *free* parameters in the equivalence relation (9). If one leaves the interlayer coupling energy ω untouched, a renormalization of the angle θ is obtained by modifying the Fermi velocity v_F . This can be achieved at the TB level by modifying the intralayer hopping in the following way:

$$V_{pp\sigma}(r_{ij}) = -t_0 \frac{\sin(\theta_{\text{MA}}/2)}{\sin(\theta/2)} e^{\delta(a_c-r_{ij})} c(r_{ij}). \quad (\text{A2})$$

In this case, two *equivalent* Hamiltonian present identical spectra in the CM limit, because $\hbar v_F k_{\hat{\theta}}$ in Eq. (8) is kept constant. A similar procedure, with additional spacial scaling to preserve the Dirac-cone value, has been employed to reduce the number of sites per unit cell in the TB modelling of TBG [25–27] and TBG-based systems [28].

Appendix B: Limits of the equivalence-class approach

The equivalence class of MATBG was robustly defined within the framework of the single-valley BM model, as reported in Sec. II. Nonetheless, the BM Hamiltonian of

Eq. (8) reasonably accounts for the ground-state electronic properties of misaligned graphene planes at stacking angles $\lesssim 10^\circ$, regardless of whether or not the bilayer structure is periodic. Indeed, a twist of $\sim 10^\circ$ entails a reciprocal space displacement of $\sim 0.3\text{\AA}^{-1}$ from the Dirac point, where the Dirac-cone bands cease to be isotropic [7]. Furthermore, the Dirac-cone approximation in graphene holds for electronic energies below ~ 0.8 eV, relative to the Fermi level. The Tight-binding simulations discussed in Sec. III suggest that more strict conditions should be imposed to guarantee an equivalence relation for MATBG. Looking at Fig. 2c, we see that two TBG structures belonging to the same equivalence class present homothetic spectral properties over a limited energy range of about ~ 40 meV around the Fermi level. In addition, we have verified that a one-to-one mapping of TBG onto MATBG is reasonably achieved for twist angles $\lesssim 6^\circ$.

On more general grounds, a TBG system of twist angle θ_m , cfr. Eq. (18), is well-represented in terms of Bloch wave functions $\psi_{n\mathbf{k}}^m(\mathbf{r}) = e^{i\mathbf{k}\cdot\mathbf{r}} u_{n\mathbf{k}}^m(\mathbf{r})$ and energy levels $\epsilon_{n\mathbf{k}}^m$, measured from the neutrality point, where n labels the band-index, $\hbar\mathbf{k}$ denotes the crystal momentum, and the functions $u_{n\mathbf{k}}^m$ have the periodicity of the commensurate TBG lattice. Roughly speaking, the weak moiré potential couples massless Dirac fermions between the single graphene layers with a mean interaction energy being much less than the unperturbed Dirac-cone energy $\hbar v_F k_{\theta_m}$. Now, given an equivalence class γ and its representative \mathcal{H}_γ , the properties of the equivalence class must be valid for $|\epsilon_{n\mathbf{k}}^m| < \frac{k_{\theta_m}}{k_{\theta_\gamma}} \hbar v_F k_{\theta_\gamma}$. Accordingly, in either TB or DFT atomistic approaches, the equivalence class of MATBG is expressed by the transformation relations

$$c_{n\mathbf{k}}^{\text{MA}} = \frac{k_{\theta_{\text{MA}}}}{k_{\theta_m}} c_{n\mathbf{k}}^m \quad u_{n\mathbf{k}}^{\text{MA}}(k_{\theta_{\text{MA}}}\mathbf{r}) = u_{n\mathbf{k}}^m(k_{\theta_m}\mathbf{r}), \quad (\text{B1})$$

which hold under the limiting condition

$$|\epsilon_{n\mathbf{k}}^m| < \frac{k_{\theta_m}}{k_{\theta_{\text{MA}}}} \hbar v_F k_{\theta_{\text{MA}}}. \quad (\text{B2})$$

Appendix C: The equivalence class of MATBG with lattice relaxation

In a real TBG system, the structure undergoes a spontaneous relaxation [60–63], which reflects the different interlayer interactions across the moiré unit cell. This effect was neglected throughout the main text, because our main goal was to identify geometric configurations exhibiting quasi-flat bands and gather them into equivalence classes.

Nonetheless, based on the arguments presented in Sec. II, and following some recent studies [31, 63, 64], we can express a CM formulation of the relaxed TBG lattice in terms of the dimensionless parameter $\alpha = \omega_{\text{AA}}/\omega_{\text{AB}} \neq 1$.

Accordingly, Eq. (5) can be rewritten as

$$\mathcal{H} = \begin{bmatrix} \hbar v_F k_\theta \boldsymbol{\sigma}_{\theta/2} \cdot \tilde{\mathbf{p}} & \omega_{AB} \tilde{\mathcal{T}}(\tilde{\mathbf{r}}) \\ \omega_{AB} \tilde{\mathcal{T}}(\tilde{\mathbf{r}})^\dagger & \hbar v_F k_\theta \boldsymbol{\sigma}_{-\theta/2} \cdot \tilde{\mathbf{p}} \end{bmatrix}, \quad (\text{C1})$$

and the Fourier coefficients of the interlayer potential acquire an additional dependence on α , namely,

$$\begin{aligned} \tilde{T}_1 &= \alpha \sigma_0 + \sigma_x, \\ \tilde{T}_2 &= \alpha \sigma_0 - \frac{1}{2} (\sigma_x - \sqrt{3} \sigma_y), \\ \tilde{T}_3 &= \alpha \sigma_0 - \frac{1}{2} (\sigma_x + \sqrt{3} \sigma_y). \end{aligned} \quad (\text{C2})$$

Then, the equivalence relation set in Eqs. (8)-(10) can be reformulated using $\gamma = \frac{\omega_{AB}}{\hbar k_\theta v_F}$. Turning to atomistic TB or DFT approaches, the treatment of relaxation effects in the search algorithm for the magic distance requires a more careful scrutiny.